

Metasurface Engineering with Tantalum Pentoxide-Coated Microspheres: Tailoring Optical Resonances and Enhancing Local Density of States

A. Fălamaș¹, A. M. M. Gherman¹, R. Vallée^{*2}, and C. Farcau^{†1}

¹National Institute for Research and Development of Isotopic and Molecular
Technologies, 65–103 Donath, 400293 Cluj-Napoca, Romania

²CNRS, University of Bordeaux, CRPP-UMR 5031, 33600 Pessac, France

Abstract

Hexagonally close-packed polystyrene (PS) microsphere monolayers coated with tantalum pentoxide (Ta_2O_5) form scalable dielectric metasurfaces that support tunable photonic resonances and enhanced local density of optical states (LDOS). Here we combine fabrication, optical and fluorescence spectroscopy, and multi-scale electromagnetic simulations to quantify how the thickness of a Ta_2O_5 shell controls far-field resonances and Rhodamine 6G (Rh6G) emission.

Experimentally, Ta_2O_5 shells of 10 nm to 70 nm deposited on PS microsphere lattices generate resonances that shift red with the thickness of the shell and systematically enhance the Rh6G fluorescence relative to flat Ta_2O_5 films. The largest integrated enhancement is obtained for 30 nm to 50 nm shells, where lattice resonances overlap the Rh6G excitation and emission bands.

Finite-cluster finite-difference time-domain simulations reproduce the measured transmittance and reflectance spectra, confirming that the fabricated lattices are well described by the geometry of Ta_2O_5 shells covering the sphere lattice. Periodic-cell simulations of single electric dipoles yield wavelength-dependent Purcell factors $F_p(\lambda)$ and directional β -factors $\beta_{\text{top}}(\lambda)$, from which we construct emission-weighted figures of merit that link LDOS modulation to the experimentally accessible top-side fluorescence enhancement.

As a complementary test of our emitter–environment model, we compare simulated and measured Purcell factors for PS/ Ta_2O_5 microsphere lattices with the same Ta_2O_5 thicknesses. A physically motivated averaging scheme that accounts for emitter position, orientation and ensemble spectral smoothing yields very good agreement across

*renaud.vallee@u-bordeaux.fr

†cfarcau@itim-cj.ro

all shells. Overall, our results establish Ta₂O₅-coated microsphere lattices as robust dielectric substrates for surface-enhanced fluorescence and clarify how shell thickness and emitter placement jointly control photonic resonances, LDOS and fluorescence response.

1 Introduction

Dielectric metasurfaces based on high-index nanostructures have emerged as versatile platforms for controlling light at the wavelength scale.[1, 2, 3] By tailoring the geometry and refractive index of subwavelength features, these structures can shape phase, amplitude and polarization and can strongly modify the local density of optical states (LDOS) seen by nearby emitters.[4, 5] In contrast to plasmonic systems, high-index dielectrics provide strong field confinement with negligible Ohmic loss, which is particularly attractive for enhanced light emission and integrated photonics.[6, 7]

For a dipole emitter coupled to a structured photonic environment, the spontaneous-emission rate $\Gamma(\lambda)$ at wavelength λ is proportional to the projected LDOS. The Purcell factor is defined as

$$F_p(\lambda) = \frac{\Gamma(\lambda)}{\Gamma_0(\lambda)} = \frac{P(\lambda)}{P_0(\lambda)}, \quad (1)$$

where Γ_0 and P_0 are the decay rate and radiated power of a reference dipole in a homogeneous medium.[4, 5] The fraction of the emitted power directed into a specific detection channel, such as the upper half-space above a metasurface, is quantified by a directional β -factor

$$\beta_{\text{top}}(\lambda) = \frac{P_{\text{top}}(\lambda)}{P(\lambda)}, \quad (2)$$

where P_{top} is the power radiated into the superstrate.

For a high-quantum-yield dye such as Rhodamine 6G (Rh6G) in a low-loss dielectric environment, non-radiative quenching is weak and the detected emission spectrum above a metasurface can be approximated as[6, 8]

$$I_{\text{det}}(\lambda) \propto S(\lambda) F_p(\lambda) \beta_{\text{top}}(\lambda), \quad (3)$$

where $S(\lambda)$ is the intrinsic emission spectrum of the dye, normalized to unit area. Equation (3) highlights that both radiative-rate enhancement and directional out-coupling determine the observed emission.

For broadband emitters, it is convenient to define emission-weighted figures of merit

$$F_p^{\text{em}} = \int S(\lambda) F_p(\lambda) d\lambda, \quad (4)$$

$$F_{p,\text{rad}}^{\text{em}} = \int S(\lambda) F_p(\lambda) \beta_{\text{top}}(\lambda) d\lambda. \quad (5)$$

For a high-yield emitter, the overall top-side emission enhancement factor is then approximately

$$E_{F,\text{top}} \simeq F_{p,\text{rad}}^{\text{em}}. \quad (6)$$

These quantities provide a direct bridge between far-field resonances observable in reflection and transmission, the near-field LDOS, and the measured fluorescence.[5]

Tantalum pentoxide (Ta_2O_5 , tantala) is a high-index dielectric with excellent optical properties in the visible and near-infrared: it combines a refractive index around 2.0–2.2 with very low absorption and a small thermo-optic coefficient.[9, 10, 11, 12, 15] Ta_2O_5 is widely used in high-reflectivity coatings for gravitational-wave detectors,[9] in low-loss waveguides and microresonators,[10, 11, 12] and more recently in high-performance metasurfaces for focusing, holography and structural colour.[15] Ta_2O_5 waveguides have also been exploited for fluorescence detection in evanescent-field configurations.[16, 17] In this context, Ta_2O_5 offers a low-loss alternative to metals for SEF, capable of enhancing local fields and LDOS without the strong non-radiative quenching typical of plasmonic substrates.[6, 7]

Self-assembled monolayers of PS microspheres form hexagonally close-packed colloidal crystals over large areas.[18] Metal films over such microsphere arrays are well-known platforms for SEF and SERS, where tunable plasmonic resonances provide strong near-field enhancement.[19, 7] Replacing the metal with a high-index dielectric overlayer could transform these systems into photonic crystals or metasurfaces that support Mie-type and guided-mode resonances.[1, 2] The resulting hybrid PS/ Ta_2O_5 shells are expected to support thickness-dependent resonances whose position and strength can be engineered to overlap a chosen emitter band.

In this work, we show that Ta_2O_5 -coated PS microsphere lattices behave as low-loss dielectric metasurfaces with tunable resonances and controllable LDOS for surface-bound dye molecules. We fabricate PS monolayers coated with Ta_2O_5 shells of 10 nm to 70 nm, characterize their optical transmission and reflection, and quantify the fluorescence enhancement. Finite-cluster FDTD simulations reproduce the measured far-field spectra when the lattices are modeled as conformal Ta_2O_5 shells, indicating that the experimental growth conditions yield shells close to this morphology. Periodic-cell simulations of single dipoles provide $F_p(\lambda)$ and $\beta_{\text{top}}(\lambda)$, from which we derive emission-weighted metrics that explain the observed thickness dependence of the fluorescence.

Finally, we validate the emitter–environment model on the same PS/ Ta_2O_5 microsphere lattice system by combining single-dipole simulations with a spatial, polarization and spectral averaging procedure detailed in the Supporting Information. This yields Purcell-factor spectra in very good agreement with experiment, linking single-emitter LDOS calculations to ensemble measurements and reinforcing the physical picture extracted from the metasurface characterization.

2 Experimental and numerical methods

2.1 Fabrication of Ta_2O_5 -coated microsphere lattices

Hexagonally close-packed PS microsphere monolayers were prepared on glass substrates following standard colloidal self-assembly protocols.[20] Monodisperse PS spheres of nominal diameters $D = 460$ nm were used. After formation of the monolayer, Ta_2O_5 was deposited by e-beam evaporation (Kenosistec KE400). The nominal Ta_2O_5 thicknesses were $t_{\text{shell}} = 10$ nm, 30 nm, 50 nm and 70 nm, as monitored by quartz crystal microbalance during

deposition.

These coatings produce hybrid PS/Ta₂O₅ shells whose effective optical thickness increases with t_{shell} . The same thicknesses were used in the simulations described below.

2.2 Optical characterization

Normal-incidence transmission and reflection spectra in the visible range were measured with a UV–vis spectrophotometer equipped with focusing optics adapted to the finite size of the microsphere patches. Transmission $T(\lambda)$ was obtained by normalizing the transmitted intensity to that of a glass reference. Reflectivity $R(\lambda)$ was measured in epi configuration and normalized to a suitable standard.

The Ta₂O₅-coated PS lattices exhibit a pronounced transmission dip accompanied by a reflectance peak, whose wavelength red-shifts with t_{shell} . This behavior is consistent with a resonance condition

$$m \lambda \simeq 2 n_{\text{eff}} d, \quad (7)$$

where m is an integer order, n_{eff} an effective refractive index, and d an effective thickness of the hybrid shell–lattice layer. Increasing t_{shell} increases $n_{\text{eff}}d$, shifting the resonance to a longer wavelength.

2.3 Fluorescence measurements

Rhodamine 6G (Rh6G) was dissolved in a 4% w/w PVP solution in ethanol and spin-coated onto the Ta₂O₅ samples and a glass reference, forming thin and nearly uniform fluorescent layers.[6] Fluorescence spectra were recorded using a micro-Raman spectrometer (B&W Tek) coupled to a microscope with a 20× objective with excitation at 532 nm. At least ten spectra were acquired at different positions from each sample, using an integration time of 1 s and five accumulations under low laser power to avoid photo-bleaching.

The fluorescence enhancement factor for each Ta₂O₅ metasurface was quantified owing to the integration performed over the measured Rh6G emission spectrum according to Eq. (5).

2.4 Time-resolved fluorescence measurements

Time-correlated single photon counting (TCSPC) measurements were performed on a time-resolved fluorescence set-up (Chimera, LightConversion, Lithuania) adapted for thin film measurements, to quantify the fluorescence lifetime of R6G spin coated onto each Ta₂O₅ metasurface, as well as onto glass slides (control samples). The samples were excited at 545 nm using a 170 fs pulsed laser with 80 kHz pulse repetition frequency laser (Pharos, LightConversion, Lithuania) obtained using an optical parametric amplifier (Orpheus, LightConversion, Lithuania) from the initial 1030 nm laser beam. The average power at the sample was 1 mW. The laser was focused using a 10x objective onto the sample and the emission signal was collected using the same objective. A 555 nm dichroic mirror and an additional 570 nm long pass filter were used to separate the emission signal from the excitation pulse. The signal was integrated over 200 s and the emission was collected in the 580-620 nm spectral range with 5 nm step size. The time-resolved fluorescence data was analyzed in

EasyTau2 software (PicoQuant, Germany) using the reconvolution fitting method, considering the instrumental response function (IRF) acquired from glass slides on the same day as the experiment. The three-dimensional data carpets acquired from the control samples were fit using mono-exponential functions, while those corresponding to the R6G spin coated onto the Ta₂O₅ metasurfaces were best fit using bi-exponential functions. Intensity weighted average lifetimes were calculated using

$$\tau_{\text{avg Int}} = \frac{\sum_{\substack{i=1 \\ J_i > 0}}^{n_{\text{exp}}} I_i \tau_i}{\sum_{\substack{i=0 \\ J_i > 0}}^{n_{\text{exp}}} I_i}. \quad (8)$$

2.5 Electromagnetic simulations

Two complementary numerical approaches were used.

First, ultraviolet–visible transmission and reflection spectra of finite Ta₂O₅-coated PS lattices and reference structures were computed with a commercial finite-difference time-domain (FDTD) solver (Lumerical FDTD).[22] The simulated geometry consisted of a cluster of 94 closely packed PS spheres forming a hexagonal patch on a SiO₂ substrate, coated with a Ta₂O₅ layer of thickness t_{shell} . PS spheres of $D = 400$ nm, 450 nm, and 500 nm were modeled with refractive index $n = 1.59$, Ta₂O₅ with $n \approx 2.0$ in the visible, and the glass substrate with $n = 1.45$. Normal-incidence plane-wave excitation and perfectly matched layers along the surface normal were used; lateral boundaries were placed sufficiently far from the cluster to avoid spurious reflections.

Second, local-emitter quantities were obtained with another time-domain Maxwell solver (Tidy3D).[23] We modeled a single unit cell of the hexagonal PS microsphere lattice on a semi-infinite SiO₂ substrate, with a conformal Ta₂O₅ shell of thickness t_{shell} surrounding the PS sphere upper halves. Periodic boundary conditions were applied laterally and perfectly matched layers along the surface normal.

Classical electric dipoles were placed either on top of Ta₂O₅ caps (sphere apices) or in the valleys between neighboring caps, representing plausible emitter locations after spin-coating. For each position, we considered in-plane (E_x) and out-of-plane (E_z) dipole orientations. The total radiated power and the power crossing a plane above the metasurface were computed and compared to a reference dipole in a homogeneous host to extract $F_p(\lambda)$ and $\beta_{\text{top}}(\lambda)$ via Eqs. (1) and (2). Emission-weighted metrics F_p^{em} and $F_{p,\text{rad}}^{\text{em}}$ were obtained by weighting with the measured Rh6G emission spectrum [Eqs. (4) and (5)].

These simulations were performed for the PS/Ta₂O₅ microsphere lattice geometries, using a PS sphere radius $R_{\text{sphere}} = 230$ nm (corresponding to $D = 460$ nm) and Ta₂O₅ shell thicknesses $t_{\text{shell}} = 10$ nm, 30 nm, 50 nm, 70 nm. Such sets of simulations allow one to grasp how the single emitter’s behaviors depend on their location and polarization with respect to the underlying surface. To further allow comparison with the performed experimental (ensemble) Purcell-factor measurements, a detailed averaging model was used, which is described in the Supporting Information (Sections S2–S8). The single-emitter responses entering that model are summarized in Fig. S3 (Emitter_Analysis).

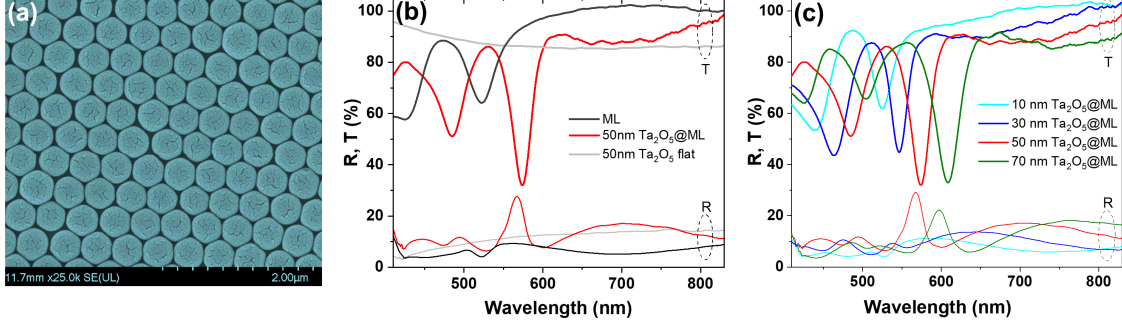


Figure 1: (a) SEM image of the two-dimensional PS microsphere monolayer. (b and c) Experimental transmission and reflectance of Ta_2O_5 -coated PS microsphere lattices. (b) Comparison between a PS monolayer, the same monolayer coated with a 50 nm Ta_2O_5 shell, and a flat 50 nm Ta_2O_5 film on glass. (c) Metasurfaces with Ta_2O_5 shell thicknesses of 10, 30, 50 and 70 nm, showing a systematic red-shift of the resonance with increasing thickness.

3 Results and discussion

3.1 Thickness-tunable resonances in Ta_2O_5 -coated lattices

Figure 1 shows the typical two-dimensional lattice structure of the PS microsphere monolayer, as it results from the well-controlled self-assembly process. The experimental transmission and reflection spectra for a bare PS microsphere monolayer, the same monolayer coated with a 50 nm Ta_2O_5 shell, and a flat 50 nm Ta_2O_5 film on glass are presented in Figure 1b-c. The PS monolayer alone exhibits a broad transmission minimum around ~ 520 nm, characteristic of Mie-type resonances of the microspheres. After coating with Ta_2O_5 , this minimum red-shifts by almost 60 nm, and the corresponding reflectance peak becomes more pronounced, signaling the formation of hybrid PS/ Ta_2O_5 photonic resonances. In contrast, the flat Ta_2O_5 film displays only smooth thin-film interference fringes without sharp features.

The same figure also presents spectra for Ta_2O_5 -coated PS lattices with $t_{\text{shell}} = 10$ nm, 30 nm, 50 nm, and 70 nm. The transmittance minima occur near 526, 547, 576, and 608 nm, respectively, demonstrating a clear and nearly monotonic red-shift with increasing shell thickness. This trend follows the simple effective-thickness picture of Eq. (7), and confirms that the Ta_2O_5 shell provides a convenient handle to tune the lattice resonance across the visible range.

Finite-cluster FDTD simulations of a Ta_2O_5 shell on a 94-sphere PS lattice reproduce these trends (Fig. 4). The simulated transmission dip and reflection peak for each shell thickness closely match the experimental positions and linewidths (Fig. S2), with residual differences attributable to fabrication tolerances and finite-size effects. The agreement supports the picture that the experimental Ta_2O_5 growth is effectively conformal at the scale relevant for the optical response.

3.2 Fluorescence enhancement and resonance alignment

Figure 2 presents representative Rh6G/PVP fluorescence spectra for the reference on glass and for Ta_2O_5 -coated PS lattices with $t_{\text{shell}} = 10$ nm, 30 nm, 50 nm and 70 nm. All metasur-

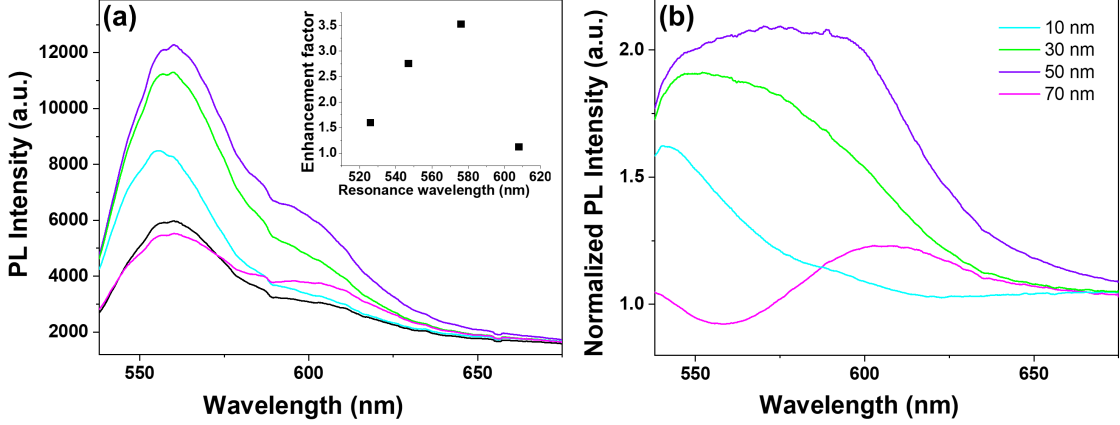


Figure 2: Fluorescence of Rh6G/PVP on Ta_2O_5 -coated PS microsphere lattices. (a) Emission spectra for metasurfaces with Ta_2O_5 shells of 10, 30, 50 and 70 nm and for the glass reference (black line). (b) Normalized enhancement spectra (sample/reference), highlighting spectral regions of maximum enhancement and their correlation with the lattice resonances. Inset: integrated fluorescence enhancement factor E_F as a function of resonance wavelength for the different shell thicknesses.

faces exhibit enhanced emission intensity relative to the glass reference. The enhancement is particularly strong for the 30 nm and 50 nm shells, consistent with their resonances falling within the Rh6G emission band and, for the thinner sample, near the excitation wavelength.

To isolate spectral shaping effects, the emission from each metasurface is divided by the reference spectrum, yielding normalized enhancement spectra. For each shell thickness, the region of maximum enhancement coincides with the transmission minimum of the corresponding lattice resonance in Fig. 1. The 10 nm shell shows enhancement mainly around ~ 540 nm, the 30 nm shell around ~ 550 nm, the 50 nm shell exhibits broad enhancement across most of the Rh6G band and centered near ~ 570 nm, and the 70 nm shell displays enhancement predominantly around ~ 605 nm. Micro-spectroscopy measurements reveal some spatial heterogeneity for the thickest shells and hints of secondary emission bands associated with higher-order photonic modes, but the global trends remain robust.

The inset of Fig. 2 summarizes the integrated enhancement factor [Eq. (5)] as a function of the measured resonance wavelength for each Ta_2O_5 thickness. The enhancement does not simply grow with increasing shell thickness. Rather, it reflects a balance between (i) excitation-field enhancement when the resonance lies close to the pump wavelength and (ii) LDOS and out-coupling enhancement when the resonance overlaps the emission band,[6, 8] as well as the spacer role of Ta_2O_5 in mitigating quenching at very small separations. The 30 nm to 50 nm shells achieve the most favorable compromise, yielding the largest integrated enhancements across the measurement conditions.

Figure 3 presents the TCSPC decay traces recorded at the emission maximum of 590 nm for Ta_2O_5 coated microsphere lattices and the control Rh6G/PVP film deposited on glass, respectively. The experimental decays are shown together with the reconvolution fits obtained using the measured IRF. The decay of the fluorophore on Ta_2O_5 metasurfaces results in a systematic reduction of the decay time, whereas fluorophores on the control sample exhibit

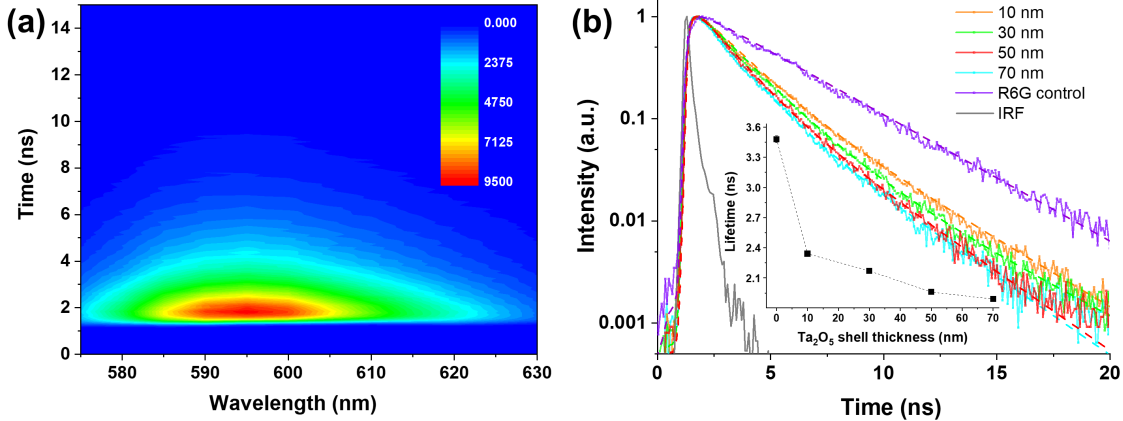


Figure 3: (a) Time-correlated single photon counting (TCSPC) data showing the three-dimensional data carpet obtained from a 50 nm shell thickness Ta_2O_5 metasurface when pumped at 545 nm. (b) Normalized kinetic traces recorded at the 590 nm emission maximum. The dotted lines represent the corresponding fitted curves. The inset shows the calculated lifetimes characteristic to the Rhodamine 6G control sample and to each metasurface with Ta_2O_5 shells of 10, 30, 50 and 70 nm.

the longest fluorescence lifetime. The average intensity-weighted lifetimes, summarized in Fig. 3b, decrease monotonically with increasing Ta_2O_5 shell thickness, from 3.48 ns for the control sample to 1.89 ns for the 70 nm coating. This progressive lifetime shortening indicates a thickness-dependent increase in the total decay rate of Rh6G, consistent with the modification of the local photonic environment and the enhanced coupling of molecular emission to photonic modes supported by the high-index Ta_2O_5 metasurface. The steady-state fluorescence enhancement and time-resolved measurements provide complementary information on the light-matter interaction in the Ta_2O_5 metasurfaces. Although the integrated fluorescence enhancement reaches a maximum for intermediate shell thicknesses (30–50 nm), the fluorescence lifetime decreases monotonically with increasing Ta_2O_5 thickness. This indicates that although thicker coatings enhance the total decay rate through increased local density of optical states, maximal detected fluorescence occurs at thicknesses where excitation-field enhancement and radiative out-coupling are optimally balanced. Thus, fluorescence enhancement in the present system is governed by the interplay between excitation enhancement, LDOS modification, and emission extraction efficiency rather than by decay-rate acceleration alone.

3.3 Finite-cluster simulation of the lattice resonances

To connect the experimental resonances to the underlying modal structure, we performed FDTD simulations of a finite-size Ta_2O_5 -coated PS cluster. Figure 4(a) schematically illustrates the simulated geometry: a hexagonal patch of PS spheres on glass, covered by a conformal Ta_2O_5 shell and residual film. Figure 4(b) compares the simulated transmission and reflection spectra of (i) a flat Ta_2O_5 film, (ii) a bare PS monolayer, and (iii) a Ta_2O_5 -coated PS monolayer for a representative shell thickness (e.g. 70 nm).

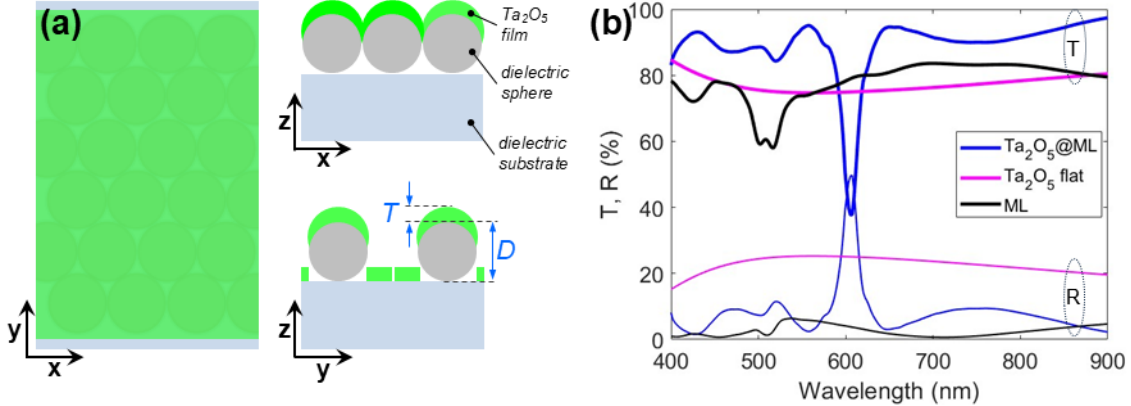


Figure 4: Finite-cluster FDTD simulations of Ta₂O₅-coated PS lattices. (a) Schematic of the simulated structure: a hexagonal cluster of PS spheres on a glass substrate coated by a Ta₂O₅ shell and residual film. (b) Simulated transmittance and reflectance spectra for a flat Ta₂O₅ film, a PS microsphere monolayer, and a Ta₂O₅-coated microsphere monolayer. The hybrid lattice exhibits a deeper and red-shifted resonance compared to the bare PS monolayer, in agreement with experiment.

The bare PS monolayer supports a modest transmission dip and a reflection peak near ~ 520 nm. Adding a Ta₂O₅ shell yields a deeper transmission minimum and stronger reflection maximum red-shifted toward 540–550 nm, consistent with the experimental red-shifts upon coating (Fig. 1). The flat Ta₂O₅ film lacks sharp resonances, showing only smooth interference fringes. Simulations of hypothetical hollow Ta₂O₅ semishells, obtained by removing the PS cores, reveal related but spectrally shifted resonances (Fig. S3). These results confirm that the sharp spectral features observed experimentally originate from the hybrid PS/Ta₂O₅, with both core and shell jointly determining the effective index and mode structure.

Electric-field maps at and away from resonance (Fig. S3) show that, at the resonance wavelength, the fields are strongly enhanced in the upper portion of the Ta₂O₅ shell and in the interstitial regions, precisely where the Rh6G/PVP layer resides. This spatial overlap provides the basis for a natural framework for interpreting the fluorescence enhancement in terms of LDOS and directional out-coupling.

3.4 Single-emitter metrics and ensemble Purcell factors

The periodic-cell simulations yield the wavelength-dependent Purcell factor $F_p(\lambda)$ and the product $F_p(\lambda)\beta_{\text{top}}(\lambda)$ for single dipoles at well-defined locations and orientations. Figure S4 in the Supporting Information summarizes these results for shell thicknesses $t_{\text{shell}} = 10$ nm, 30 nm, 50 nm, 70 nm, with panels distinguishing emitters on caps vs between caps and in-plane vs out-of-plane dipole orientations.

Several trends emerge. First, for all thicknesses the averaged ($F_p^{\text{em}} = \langle F_p \rangle$, Eq. (4)) in-plane dipoles generally experience larger F_p than out-of-plane ones, especially when located on cap of the spheres, but also between caps for larger thicknesses of the coating layer. This reflects the predominantly tangential character of the hybrid lattice modes. Second, the product $F_p\beta_{\text{top}}$, which controls the contribution to top-side emission [Eq. (3)], is maximized

for in-plane dipoles located on or near the upper Ta_2O_5 caps for intermediate thicknesses (30 nm to 50 nm). Third, the spectral position of the $F_p \beta_{\text{top}}$ maximum shifts to longer wavelengths as t_{shell} increases, tracking the resonance movement in Fig. 1.

When these single-emitter responses are integrated over the Rh6G emission spectrum to form $F_{\text{p,rad}}^{\text{em}}$ [Eq. (5)], the resulting values show the same qualitative thickness dependence as the measured fluorescence enhancement E_F in Fig. 2. In particular, the intermediate Ta_2O_5 thicknesses provide the best compromise between LDOS enhancement and efficient out-coupling into the upper half-space for emitters located near the top of the shells. This picture is consistent with the experimental observation that the 30 nm to 50 nm shells yield the largest integrated enhancement.

3.5 Purcell factor for PS/ Ta_2O_5 microsphere lattices: theory vs experiment

To establish an emitter–environment model and quantify how single-dipole responses translate into ensemble measurements, we consider the PS/ Ta_2O_5 microsphere lattice with the same Ta_2O_5 shell thicknesses as studied above. For this geometry, the experimental observable—the Purcell factor extracted from fluorescence lifetime measurements—averages over a large number of emitter configurations, making it an ideal benchmark for an averaging framework.

We model a PS sphere of radius $R_{\text{sphere}} = 230$ nm (nominal diameter $D = 460$ nm) coated with a Ta_2O_5 shell of thickness $t_{\text{shell}} \in \{10, 30, 50, 70\}$ nm. Dye emitters are assumed to be distributed on the outer shell surface, either on the spherical caps (high-curvature regions) or in the valleys between caps, as motivated by the wetting and drying dynamics during spin-coating. For each placement, we compute $F_p(\lambda)$ for in-plane and out-of-plane dipole orientations, and then construct an averaged Purcell factor $\langle F_P(\lambda) \rangle$ that accounts for (i) the probability of being on a cap vs between caps, (ii) random dipole orientation, and (iii) ensemble spectral smoothing. Details of this averaging model are given in Sections S3–S7 of the Supporting Information.

In compact form, the spatially and polarization-averaged Purcell factor reads

$$\langle F_P(\lambda) \rangle = P_{\text{on}} \langle F_P^{\text{on}}(\lambda) \rangle_{\text{pol}} + P_{\text{bet}} \langle F_P^{\text{bet}}(\lambda) \rangle_{\text{pol}}, \quad (9)$$

where P_{on} and $P_{\text{bet}} = 1 - P_{\text{on}}$ denote the probabilities for an emitter to reside on a cap or between caps, respectively, and the polarization averages follow the standard isotropic weighting (two transverse and one longitudinal component). The probabilities are modeled as a logistic function of the dimensionless curvature ratio $t_{\text{shell}}/R_{\text{sphere}}$, derived from a two-state Boltzmann partition between capillary suction into the interstices and contact-line pinning on the caps [25, 24], and constrained by a global optimization across all four shell thicknesses (see SI).

In addition, we introduce two per-thickness corrections when comparing to experimental data: (i) a spectral smoothing factor $s \in [0, 1]$ that damps oscillations present in single-geometry simulations but absent in ensemble measurements, and (ii) a small wavelength shift $\Delta\lambda$ that accounts for modest discrepancies between nominal and actual shell thicknesses and refractive indices. The full model is

$$F_P^{\text{model}}(\lambda) = \overline{F}_P + s[\langle F_P(\lambda + \Delta\lambda) \rangle - \overline{F}_P], \quad (10)$$

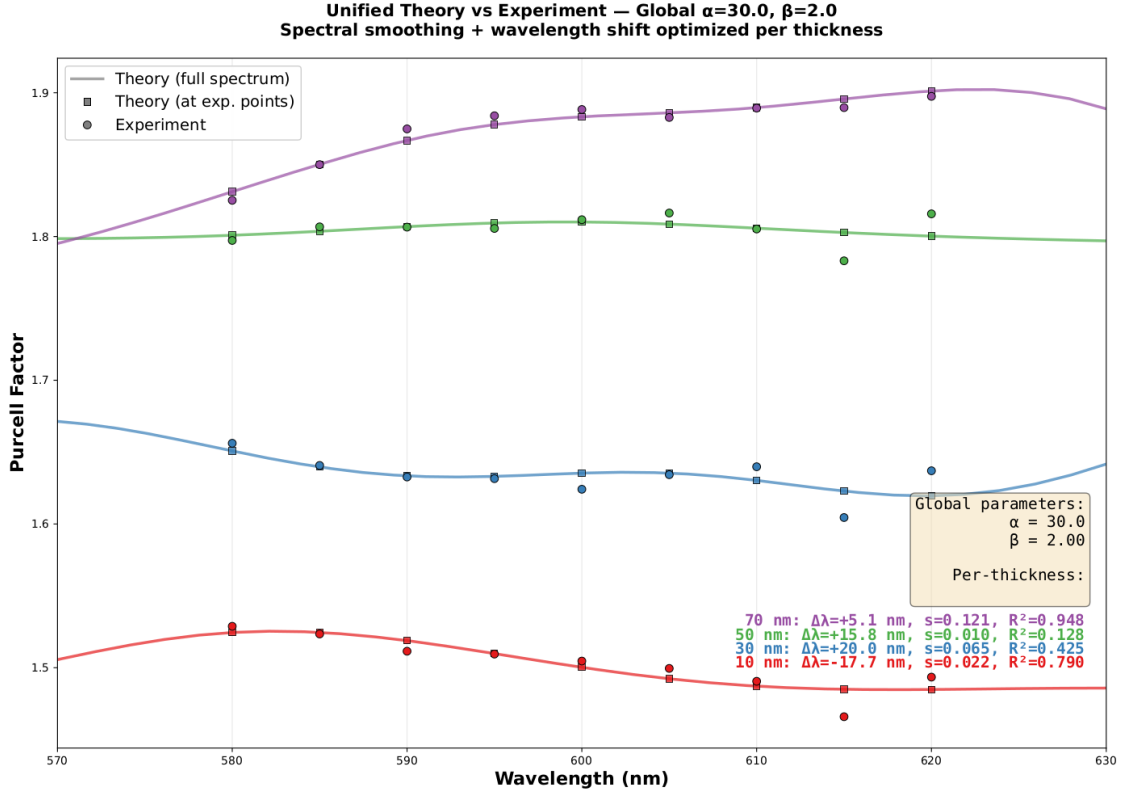


Figure 5: Comparison between the modeled Purcell factor (solid lines) and experimental data (circles) for PS/Ta₂O₅ microsphere lattices with Ta₂O₅ shell thicknesses of 10, 30, 50 and 70 nm (bottom to top). Squares indicate the model evaluated at the experimental wavelengths. Global curvature parameters are shared across all thicknesses; per-thickness smoothing factors s and wavelength shifts $\Delta\lambda$ are indicated in the inset.

where \bar{F}_P is the spectral average of $\langle F_P \rangle$ over the measured wavelength range. Global parameters controlling the curvature dependence are shared across all thicknesses, while s and $\Delta\lambda$ are adjusted per shell.

Figure 5 compares the resulting $F_P^{\text{model}}(\lambda)$ to the experimentally extracted Purcell factors for PS/Ta₂O₅ microsphere lattices with $t_{\text{shell}} = 10, 30, 50, 70$ nm. The agreement is very good for the 70 nm and 10 nm shells, with coefficients of determination R^2 close to 0.95 and 0.8, respectively, and remains qualitatively correct for intermediate thicknesses. The optimized curvature parameters yield a monotonic increase of the on-cap probability from ~ 0.05 at 10 nm to ~ 0.74 at 70 nm, consistent with the progressive filling of the interstices and the resulting loss of capillary suction as the shell thickness grows (see SI for details). The small smoothing factors $s < 0.13$ indicate that the experimental spectra effectively average over a very large number of geometric configurations, far exceeding the discrete set sampled in the simulations.

This agreement shows that the same physical ingredients that control emitter–lattice coupling in the Ta₂O₅-coated PS metasurfaces—namely, the spatial distribution of emitters relative to high-LDOS regions, dipole orientation averaging, and ensemble spectral smoothing—govern the Purcell factors measured on the microsphere lattices. The single-emitter responses

summarized in Fig. S4 thus provide a consistent foundation for interpreting both types of experiments.

4 Conclusions

We have presented a combined experimental and numerical study of Ta₂O₅-coated PS microsphere lattices as dielectric metasurfaces for surface-enhanced fluorescence. Ta₂O₅ shells of thickness 10 nm to 70 nm deposited on PS monolayers produce tunable photonic resonances that red-shift with increasing thickness and significantly enhance Rh6G fluorescence compared to flat Ta₂O₅ films. The largest integrated enhancements are obtained for 30 nm to 50 nm shells, where the lattice resonances overlap the Rh6G excitation and emission bands, and where the Ta₂O₅ acts as an optimal spacer.

Finite-cluster FDTD simulations show that the experimental far-field spectra are well reproduced by a conformal Ta₂O₅ shell covering the PS spheres and interstices, confirming that this geometry captures the relevant optical thickness and field distributions. Periodic-cell dipole simulations in the same geometry yield wavelength-dependent Purcell factors and directional β -factors, from which emission-weighted metrics can be constructed. The resulting thickness dependence of the radiative LDOS and of the top-side emission enhancement agrees qualitatively with the measured fluorescence enhancement and highlights the key role of emitters located in the upper Ta₂O₅ shell.

A complementary comparison between simulated and experimental Purcell factors for PS/Ta₂O₅ microsphere lattices, using a simple but physically grounded averaging model, further validates the emitter–environment description. This unified framework—combining Ta₂O₅ shell modelling, periodic-cell dipole simulations and ensemble averaging grounded in capillary energy-barrier arguments—provides a quantitative route to designing Ta₂O₅-based metasurfaces with tailored LDOS and emission properties.

More broadly, our results demonstrate that Ta₂O₅-coated microsphere lattices constitute a robust and low-loss SEF platform whose photonic resonances and LDOS can be engineered via simple geometric parameters, such as microsphere diameter and shell thickness. The Ta₂O₅ geometry naturally integrates with planar Ta₂O₅ photonics,[10, 13, 14] and provides a promising route toward large-area, CMOS-compatible dielectric metasurfaces for fluorescence enhancement, sensing and light–matter interaction engineering.

Acknowledgements

This work was supported by a grant of the Romanian Ministry of Research, Innovation and Digitalization (MCID), CCDI–UEFISCI, project number PN-IV-P8-8.3-PM-RO-FR-2024-0163, within PNCDI IV. Authors from INCDTIM also acknowledge the “Nucleu” Program within the National Plan for Research, Development and Innovation 2022–2027, project PN 23 24 01 02. The authors thank I. Cardan and D. Cuibus for help with preparing microsphere arrays.

References

- [1] Kuznetsov, A. I.; Miroschnichenko, A. E.; Brongersma, M. L.; Kivshar, Y. S.; Luther-Davies, B., Optically resonant dielectric nanostructures, *Science*, **2016**, 354(6314), aag2472.
- [2] Staude, I.; Schmid, J., Metamaterial-inspired silicon nanophotonics, *Nat. Photonics*, **2017**, 11, 274–284.
- [3] Liu, W.; Kivshar, Y. S., Multipolar interference effects in nanophotonics, *Philos. Trans. A Math. Phys. Eng. Sci.*, **2017**, 375(2090), 20160317.
- [4] Novotny, L.; Hecht, B., *Principles of Nano-Optics*, Cambridge University Press, **2012**.
- [5] Lodahl, P.; Mahmoodian, S.; Stobbe, S., Interfacing single photons and single quantum dots with photonic nanostructures, *Rev. Mod. Phys.*, **2015**, 87(2), 347–400.
- [6] Lakowicz, J. R., *Principles of Fluorescence Spectroscopy*, Springer, Boston, 3rd edn, **2006**.
- [7] Kühn, S.; Hakanson, U.; Rogobete, L.; Sandoghdar, V., Enhancement of Single-Molecule Fluorescence Using a Gold Nanoparticle as an Optical Nanoantenna, *Phys. Rev. Lett.*, **2006**, 97, 017402.
- [8] Lodahl, P.; van Driel, A. F.; Nikolaev, I. S.; Irman, A.; Overgaag, K.; Vanmaekelbergh, D.; Vos, W. L., Controlling the dynamics of spontaneous emission from quantum dots by photonic crystals, *Nature*, **2004**, 430, 654–657.
- [9] Steinlechner, J., Development of mirror coatings for gravitational-wave detectors, *Philos. Trans. R. Soc. A*, **2018**, 376, 20170282.
- [10] Belt, M.; Davenport, M. L.; Bowers, J. E.; Blumenthal, D. J., Ultra-Low-Loss Ta₂O₅-core/SiO₂-clad planar waveguides on Si substrates, *Optica*, **2017**, 4(5), 532–535.
- [11] Wang, T.-J.; Chen, P.-K.; Li, Y.-T.; Sung, A.-N., Athermal high-Q tantalum-pentoxide-based microresonators on silicon substrates, *Opt. Laser Technol.*, **2021**, 138, 106925.
- [12] Subramanian, A. Z.; Oton, C. J.; Wilkinson, J. S.; Greef, R., Waveguiding and photoluminescence in Er³⁺-doped Ta₂O₅ planar waveguides, *J. Luminesc.*, **2009**, 129(8), 812–816.
- [13] Liu, Z.; Yao, W.; You, M.; Yu, X.; Ding, N.; Cheng, W.; Li, Z.; Tang, X.; Guo, F.; Zhao, Q., Tantalum Pentoxide Integrated Photonics: A Promising Platform for Low-Loss Planar Lightwave Circuits with Low Thermo-Optic Coefficients, *ACS Photonics*, **2025**, 12(3), 684–695.
- [14] Brodnik, G. M.; Spektor, G.; Williams, L. M.; Zhang, J.; Carollo, A. R.; Dan, A.; Black, J. A.; Carlson, D. R.; Papp, S. B., Monolithic 3D integration of tantalum pentoxide photonics on arbitrary substrates, arXiv:2509.08092, **2025**.

- [15] Zhang, C.; Chen, L.; Lin, Z.; Song, J.; Wang, D.; Li, M.; Koksai, O.; Wang, Z.; Spektor, G.; Carlson, D.; Lezec, H. J.; Zhu, W.; Papp, S.; Agrawal, A., Tantalum pentoxide: a new material platform for high-performance dielectric metasurface optics in the ultraviolet and visible region, *Light Sci. Appl.*, **2024**, 13, 23.
- [16] Schmitt, K.; Oehse, K.; Sulz, G.; Hoffmann, C., Evanescent field sensors based on tantalum pentoxide waveguides – A review, *Sensors*, **2008**, 8(2), 711–726.
- [17] Grandin, H. M.; Städler, B.; Textor, M.; Vörös, J., Waveguide excitation fluorescence microscopy: a new tool for sensing and imaging the biointerface, *Biosens. Bioelectron.*, **2006**, 21(8), 1476–1482.
- [18] Mie, G., Beiträge zur Optik trüber Medien, speziell kolloidaler Metallösungen, *Annalen der Phys.*, **1908**, 330(3), 377–445.
- [19] Nechita, N.; Farcau, C.; Tuning plasmons of metal-coated microsphere arrays towards optimized surface-enhanced spectroscopy, *Optics Express* **2021**, 29(25), 42238–42250.
- [20] Zhang, J-T.; Wang, L.; Lamont, D. N; Velankar, S. S.; Asher, Sanford A., Fabrication of large-area two-dimensional colloidal crystals, *Angew. Chem. Int. Ed.*, **2012**, 51(25), 6117–6120.
- [21] Bidault, S.; Devilez, A.; Ghenuche, P.; Stout, B.; Bonod, N.; Wenger, J., Competition between Förster Resonance Energy Transfer and Donor Photodynamics in Plasmonic Dimer Nanoantennas, *ACS Photonics*, **2016**, 3(5), 895–903.
- [22] Ansys Lumerical FDTD Simulation of Photonic Components, <https://www.ansys.com/products/optics/fdtd>.
- [23] Flexcompute Inc., Tidy3D Electromagnetic Solver, <https://www.flexcompute.com/tidy3d/>.
- [24] P.-G. de Gennes, F. Brochard-Wyart, and D. Quéré, *Capillarity and Wetting Phenomena: Drops, Bubbles, Pearls, Waves*, Springer, New York (2004).
- [25] H. A. Kramers, “Brownian motion in a field of force and the diffusion model of chemical reactions,” *Physica* **7**, 284–304 (1940). doi:10.1016/S0031-8914(40)90098-2